Transp Porous Med (2010) 83:289–318
DOI 10.1007/s11242-009-9440-z

Simulation of Solute Transport Through Fractured Rock: A Higher-Order Accurate Finite-Element Finite-Volume Method Permitting Large Time Steps

Stephan K. Matthäi · Hamidreza M. Nick · Christopher Pain · Insa Neuweiler

Received: 24 March 2009 / Accepted: 19 June 2009 / Published online: 10 July 2009

Abstract Discrete-fracture and rock matrix (DFM) modelling necessitates a physically realistic discretisation of the large aspect ratio fractures and the dissected material domains. Using unstructured spatially adaptively refined finite-element meshes, we find that the fastest flow often occurs in the smallest elements. Flow velocity and element size vary over many orders of magnitude, disqualifying global Courant number (CFL)-dependent transport schemes because too many time steps would be necessary to investigate displacements of interest. Here, we present a higher-order accurate implicit pressure–(semi)-implicit transport scheme for the advection–diffusion equation that overcomes this CFL limitation for DFM models. Using operator splitting, we solve the pressure and the transport equations on finite-element, node-centred finite-volume meshes, respectively, using algebraic multigrid methods. We apply this approach to field data-based DFM models where the fracture flow velocity and mesh refinement is 2–4 orders of magnitude greater than that of the matrix. For a global CFL of $\leq$10,000, this implies sub-CFL, second-order accurate behaviour in the matrix, and super-CFL, at least first-order accurate, transports in fast-flowing fractures. Their greater refinement, however, largely offsets this numerical dispersion, promoting a

S. K. Matthäi
Department of Mineral Resources and Petroleum Engineering, Montan University of Leoben, Max Tendler Str. 4, 8700 Leoben, Austria
e-mail: stephan.matthai@unileoben.ac.at

H. M. Nick (✉) · C. Pain
Department of Earth Science and Engineering, Imperial College London, South Kensington Campus, Exhibition Road, London SW7 2AZ, UK
e-mail: h.maghami-nick07@imperial.ac.uk

C. Pain
e-mail: c.pain@imperial.ac.uk

I. Neuweiler
Institute of Fluid Mechanics and Environmental Physics in Civil Engineering, Appelstrae 9A, 30167 Hannover, Germany
e-mail: Aeuweiler@hydromech.uni-hannover.de

highly accurate overall solution. Numerical and fracture-related mechanical dispersions are compared in the realistic DFM models using second-order accurate runs as reference cases. With a CFL histogram, we establish target error criteria for CFL overstepping. This analysis indicates that for extreme fracture heterogeneity, only a few transport steps can be sufficient to analyse macro-dispersion. This makes our implicit method attractive for quick analysis of transport properties on multiple realisations of DFM models.

Keywords FEM · FVM · Hybrid element · Unstructured mesh · Discrete fracture and matrix model · DFN · DFM · Solute transport · Passive tracer advection · Dispersion

1 Introduction

Prediction of transport processes in highly heterogeneous systems, such as fractured rock, is usually difficult due to the complex spatial correlation structure and the large variations of permeability and porosity. Numerical models have the potential to predict large-scale flow and transport behaviour in such systems using only sparse observations.

Arguably, fit-for-purpose models of fractured rock need to be very complex to be predictive, and are therefore restricted to the small scale unless special provisions for computational efficiency can be made. Also, the models need to be highly geometrically flexible so that complex intersections of fractures and the resulting complex-shaped matrix blocks can be discretised with small cells, while larger parts of the rock matrix can be meshed coarsely, cf. Paluszny et al. (2007), Matthäi et al. (2007b). It will be shown here that such flexible meshes also require a sophisticated time discretisation, as global time-step criteria lead to the requirement of very small time steps, making simulations unreasonably slow.

One problem with simulations of processes in fractures is that simulation models based on regular or structured grids cannot represent inclined or curved intersecting fractures or faults with variable orientations. Therefore, such simulation models rely on idealisations of the flow geometry and averages from discrete fracture network models (DFN, e.g. Derschowitz et al. 1998). However, it is questionable whether these models retain the velocity spectra relevant for transport simulations (Matthäi and Belayneh 2004).

Recently, many advanced finite-element finite-volume techniques have been developed to simulate fluid flow and solute transport in heterogeneous porous media (Aziz and Settari 1979; Aziz 1993; Cordes and Kinzelbach 1992; Durlofsky 1993; Mose et al. 1994; Huber and Helmig 1999, 2000; Juanes et al. 2002; Geiger 2004; Matthäi et al. 2007b). Hybrid methods for multiphase fluid flow were presented as well (Hoteit and Firoozabadi 2005; Eikemo et al. 2009; Natvig and Lie 2008). Unstructured grid, combined finite-element finite-volume approaches for advection–diffusion problems go back to Baliga's thesis in 1978 (Baliga 1978; Baliga and Patankar 1980). They were the first to recognize the concept of control-volume stencils which we have generalised to hybrid finite-element meshes with material discontinuities (Paluszny et al. 2007). Our new hybrid element stencils allow the assembly of finite volumes from arbitrary combinations of tetrahedral, prism, pyramid and hexahedral elements.

However, the paucity of publications that demonstrate a successful application of transport simulations to realistic field data-based fracture geometries is striking. One reason for this may be the dependence of these simulation schemes on the Courant–Friedrich–Levy condition. In the context of fracture flow, this restricts time-stepping to prohibitively small increments because the smallest finite-elements and control volumes tend to coincide with the fast-flowing fracture intersections as will be shown below.

In this article, we present a new higher-order accurate transport scheme for combined finite-element node-centred finite-volume (FEM–FVM) meshes with discrete representations of the fractures and the rock matrix (DFM), as opposed to fracture-only DFN models. In our DFM models, the fractures are treated as discrete surface or volumetric entities with internal degrees of freedom and embedded in a consistent matrix mesh (Paluszny et al. 2007). The severe CFL constraint associated with fracture–matrix transport is overcome by making the calculations implicit or semi-implicit. The proposed method is bounded and higher-order accurate in space and time, largely eliminating numerical dispersion from transport calculations. This will be confirmed by comparing the results of time-consuming second-order accurate runs conducted on field data-based DFM models with super CFL results obtained with the proposed implicit method. CFL histograms will be used to establish a criterion for CFL overstepping.

This article begins with a presentation of the governing equations, their discretisation in space and time, and the higher-order accurate transport scheme including a consistency mapping of the transported variable from the finite-volume to the finite-element discretisation. Then, several field data-based DFM models are used to illustrate the characteristic behaviour of the method for passive tracer advection and to evaluate the numerical dispersion which occurs when global CFL is exceeded. This includes the presentation of an original cross-sectional sampling/integration procedure for the hybrid finite-element finite-volume meshes.

2 Methods

This section presents the governing equations and their discretisation scheme in space and time. It includes the presentation of our new higher-order accurate transport scheme. Tables 1 and 2 explain the notation used in this article. The computational algorithms presented below are implemented in the CSMP++ application programmer interface (Matthäi et al. 2004, 2007b) and are freely available for non-commercial use.

2.1 Governing Equations

Like Durlofsky (1993) or Huber and Helmig (1999), we compute transient fluid pressure diffusion and the advection–diffusion of a tracer in a sequential manner: First, an elliptic–parabolic pressure equation is solved to obtain the interstitial flow velocity, $\mathbf{v_i}$, from the gradient in fluid pressure, p, via Darcy's law, taking into account the fluid density variations due to the presence of the solute, ρ. After that, the advection–diffusion equation describing solute transport with the flow field is solved.

2.1.1 Pressure Equation

The Darcy velocity in a porous medium, $\mathbf{v}$ (m/s), is

$$\mathbf{v} = -\frac{\mathbf{k}}{\mu} \left(\nabla p - \rho\, \mathbf{g}\right), \tag{1}$$

and the vector $\mathbf{g}$ represents the acceleration due to gravity (9.81 kg/s^2) acting opposite to the vertical direction, $\mathbf{k}$ is the hydraulic conductivity tensor (m^2), μ is the dynamic viscosity of water (kg/m s) and ρ is its density (kg/m^3). The variable p is the water pressure (kg/m s^2).

Table 1 Notation used in text and figures

Symbol	Unit	Explanation
$\mathbf{A}\,\mathbf{x} = \mathbf{b}$		Global solution matrix, solution- and right-hand vectors
DN		Matrix of spatial derivatives of finite-element interpolation functions
N		Vector of finite-element interpolation functions
M		Vector of finite-volume interpolation functions
A	m^2	Area of finite-volume facet
$\bar{c}$	$\mathrm{kg\ m}^{-3}$	c discretised in piecewise constant finite-volume framework
$\hat{c}$	$\mathrm{kg\ m}^{-3}$	c discretised in piecewise linear finite-element framework
$\tilde{c}$	$\mathrm{kg\ m}^{-3}$	$\hat{c}$ interpolated to finite-volume integration points
(e)		Finite element (as used to discern integral contributions to **A**)
(fv)		Finite volume (as used in corresponding integrals)
H()		Heaviside function
$i,\ j$		Element and node indices in matrix equations
k		Index for finite-volume facets
n		Time level or number of elements
n		Unit normal to finite-volume facet
p		Picard iteration level
f		Number of facets surrounding one finite volume
S	m^2	Surface (as used in integrals, etc.)
$u,\ c,\ d$		Upstream, current, and downstream finite volumes
V	m^3	Volume (as used in integrals, and to calculate pore volume)
V_f	m^3	Fracture volume
V_m	m^3	Matrix volume
$\bar{q}$	$\mathrm{kg\ m}^{-3}\ \mathrm{s}^{-1}$	Source/sink on the discretised finite volume
q_f	$\mathrm{m}^3\ \mathrm{s}^{-1}$	Fracture flux
q_m	$\mathrm{m}^3\ \mathrm{s}^{-1}$	Matrix flux
q_v	$\mathrm{m}^3\ \mathrm{s}^{-1}$	Block scale Darcy volume flux
Variables used in the spatio-temporal flux limiting		
φ		Control parameter for Θ-time differencing
Ω		Distribution parameter for divergence terms between **A** and **b**
σ_j		Parameter used in the determination of Ω values
Θ		Temporal limiter value for higher-order fluxes
U	X	Advected variable normalised by local value range
U_k	$\mathrm{m}^3\ \mathrm{s}^{-1}$	U Interpolated to boundary k of finite volume
$\tilde{U_k}$	$\mathrm{m}^3\ \mathrm{s}^{-1}$	Spatially NVD limited value of U_k
ξ		Slope limiter value (scheme is TVD when $\xi = 2$)

The dynamics of pressure in a transient slightly compressible flow problem are captured by the volume balance equation for the water

$$c_t \frac{\partial p}{\partial t} = \nabla \cdot \left[\frac{\mathbf{k}}{\mu} (\nabla p - \rho\, \mathbf{g}) \right] + \dot{q}, \tag{2}$$

Table 2 Physical variables used in the pressure-concentration formulation

Symbol	Unit	Explanation
$\mathbf{c}_t$	Pa^{-1}	Total system compressibility
β_w	Pa^{-1}	Compressibility of the water
β_s	Pa^{-1}	Compressibility of the solid phase (porous material)
F	$\mathrm{kg\ m}^{-2}\ \mathrm{s}$	Solute flux
$\mathbf{g}$	$\mathrm{m\ s}^{-2}$	Acceleration of gravity vector (pointing downward)
$\mathbf{k}$	m^2	Permeability tensor
k_n	m^2	Permeability projected onto FV facet normal
μ	Pa s	Dynamic viscosity of fluid
p	Pa	Absolute fluid pressure
ϕ	X	Porosity (of the solid rock, including the void space in fractures)
c	$\mathrm{kg\ m}^{-3}$	Concentration of transported variable
q	$\mathrm{m}^3\ \mathrm{kg\ m}^{-3}\ \mathrm{s}^{-1}$	Mass source or sink
$\dot{q}$	s^{-1}	Source or sink rate
ρ	$\mathrm{kg\ m}^3$	Density of fluid
t	s	Time
$\mathbf{v}$	$\mathrm{m\ s}^{-1}$	Darcy velocity
$\mathbf{v}_i$	$\mathrm{m\ s}^{-1}$	Interstitial velocity ($\mathbf{v}/\phi$)

where $\dot{q}$ stands for external sinks and sources (1/s) and the left-hand multiplier, c_t, is the total system compressibility ($\mathrm{ms}^2/\mathrm{kg}$)

$$c_t = \phi\beta_w + (1-\phi)\beta_s \tag{3}$$

representing the storage coefficient. It is a function of the compressibilities of the water, β_w, and the porous material, β_s. The c_t affects the hydraulic diffusivity of the system, $\kappa_p = k/(\mu\phi c_t)$, and a special treatment is applied to fractures because they exhibit a non-linear relationship between fracture length and c_t (Matthäi et al. 1998).

2.1.2 Transport Equation

Once the velocity distribution in the flow domain has been established, we calculate the solute transport by solving the advection–diffusion equation

$$\phi\frac{\partial c}{\partial t} + \nabla\cdot\mathbf{J} = \phi\frac{\partial c}{\partial t} + \nabla\cdot[\mathbf{v}c - \mathbf{D}\nabla c] = q. \tag{4}$$

c ($\mathrm{kg/m}^3$) stands here for the solute concentration, D (m^2/s) is the diffusion coefficient for the solute in water and q stands for external sinks and sources. $\mathbf{J}$ is the flux of concentration. Note that the flow velocity is not necessarily divergence free because we consider transient flow of slightly compressible water.

2.2 Finite-Element Finite-Volume Discretisation

We simulate solute transport in fractured rock or otherwise highly heterogeneous porous media that are discretised with spatially variably refined unstructured grids to allow a realistic representation of the flow geometry. Making use of the technique of operator splitting, we solve the pressure equation on a linear finite-element discretisation, similar to Huber and Helmig (1999, 2000) and Firoozabadi and co-workers (Karimi-Fard and Firoozabadi 2003; Monteagudo and Firoozabadi 2004). The transport equation is solved using a conservative finite-volume method discretised on a finite-volume mesh that is constructed around the nodes of the finite-element mesh (Fig. 1). In this approach, the solute fluxes over the finite-volume interfaces, F, are evaluated using the properties of the finite-element calculations. Finite elements and finite volumes assume a complementary role in the spatio-temporal integration of fluid pressure and concentration, respectively. The method allows to achieve flux continuity and conservation of fluid volume, while keeping the advantages of flexible grids. The finite-volume mesh is realised only in parametric space using a new completely general node-centred finite-volume tesselation. This method works for any combinations of tetrahedral, prism, pyramid, hexahedral and surface elements, see Paluszny et al. (2007). In this framework, the transport equation (4) is integrated over each finite volume. The divergence of the flux is then transformed into a surface integral:

$$\int_{\text{volume}} \nabla \cdot \mathbf{J} dR = - \int_{\text{surface}} \mathbf{n} \cdot \mathbf{J} dR. \tag{5}$$

The fluxes, F, therefore have to be evaluated at the cell interfaces. Such a finite-volume discretisation that places cell interfaces (hereafter called *facets*, see Fig. 2) into the centre of finite elements, where their interpolation function derivatives are nearly exact, correctly integrates the discontinuous velocity field that arises from the differentiation of these piecewise linear element interpolation functions, see Cordes and Kinzelbach (1992).

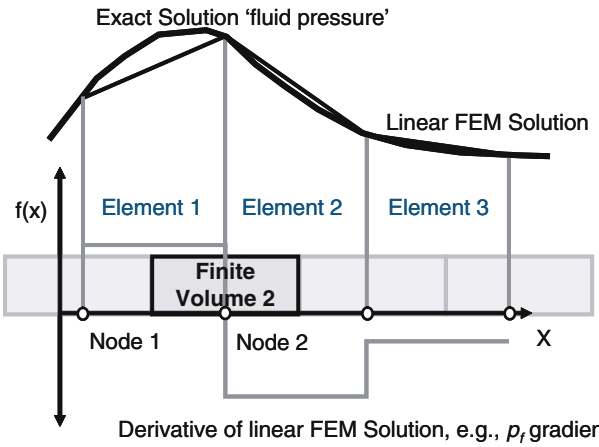

Fig. 1 One-dimensional dual mesh finite-element finite-volume discretisation of a Darcian fluid flow. Fluid pressure is discretised using the piecewise linear finite-element basis functions. This leads to a piecewise constant pressure derivative that is discontinuous across element boundaries, but exact at element centres where it is used to compute the surface-normal fluxes in- and out of node-centred finite volume cells. Thus, finite-volume surface integration achieves flux continuity in spite of the low order of discretisation

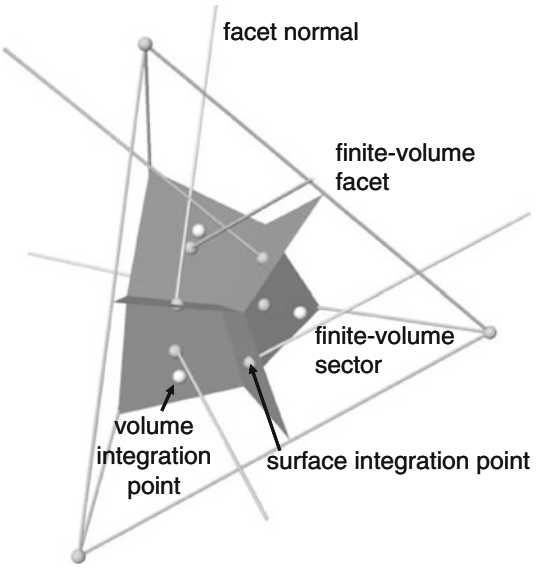

Fig. 2 Internal surfaces, surface normals, and surface and volume integration points for the linear tetrahedron. The surfaces constitute the walls of the node centred finite volume. The volume integration points are needed for the bijective mapping and to compute distributed source and sink terms

Using this new discretisation, the distributed dependent variable (for instance concentration, c), as discretised with piecewise constant interpolation functions M over the finite volumes, $\bar{c}$, is not exactly equivalent when integrated over the entire model domain to $\hat{c}$, discretised with piecewise linear functions N on the finite elements. For consistency, a projection is required mapping finite-volume variables to finite-element nodes once a transport step has been completed.

$$\begin{aligned} \hat{c}(x, y, z, t) &= \sum_{j=1}^{n} N_j(x, y, z)\, \hat{c}_j(t), \\ \bar{c}(x, y, z, t) &= \sum_{j=1}^{n} M_j(x, y, z)\, \bar{c}_j(t). \end{aligned} \tag{6}$$

This L^2-projection of c from the finite-volume to the finite-element discretisation is obtained by solving the global matrix equation

$$\begin{aligned} \hat{c}(t) &= \mathbf{B}^{-1}\, \mathbf{P}\, \bar{c}(t), \\ \mathbf{B} &= \int N_i N_j \, \mathrm{d}V, \\ \mathbf{P} &= \int N_i M_j \, \mathrm{d}V. \end{aligned} \tag{7}$$

The results of this projection are illustrated for a step function in Fig. 3. In the remainder of the article, symbols with hat are used for the finite-element formulation, while symbols with overbar are used for the finite-volume formulation.

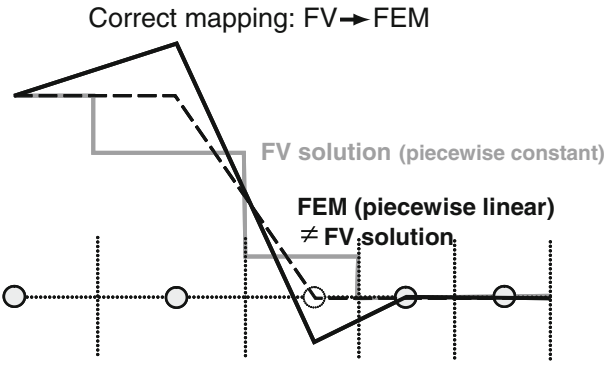

Fig. 3 One-dimensional bijective mapping of a step function from the finite volume to the finite-element discretisation. Note over- and under-shoots that arise in the finite-element description next to the discontinuity due to its approximation with piecewise linear functions

2.3 Solution Procedure

Operator splitting is used to solve the pressure equation with the finite-element method and the transport equation with the finite-volume method except for diffusive contributions to the fluxes which are also computed using the FEM.

2.3.1 Finite-Element Discretisation of the Pressure Equation

As outlined above, the pressure equation (2) is solved using the standard Bubnov–Galerkin finite-element method. Trilinear element interpolation functions N_j are used to approximate the integration of fluid pressure in space and are equivalent to the nodal weights W_j. The fluid pressure is evolved using an implicit (Backward–Euler) integration of time:

$$[\mathbf{C} + \triangle t\, \mathbf{K}]\, \mathbf{p_{t+\triangle t}} = \mathbf{C}\, \mathbf{p_t} + \triangle t\, [\mathbf{G} + \mathbf{Q}]\,, \tag{8}$$

where **G** and **Q** accumulate gravitational terms and fluid sources and sinks, respectively.

The capacitance and conductance matrices **C** and **K** contain the contributions of individual finite elements, (e), in the domain of interest:

$$\mathbf{C} = \sum_i^n \int_{(e)_i} \mathbf{N^T}\, c_t\, \mathbf{N} \mathrm{d}V,$$

$$\mathbf{K} = \sum_i^n \int_{(e)_i} \nabla \mathbf{N^T}\, \frac{\mathbf{k}}{\mu}\, \nabla \mathbf{N} \mathrm{d}V,$$

$$\mathbf{G} = \sum_i^n \int_{(e)_i} \mathbf{N^T}\, \rho \frac{k_z}{\mu}\, \mathbf{g}\, \nabla \mathbf{N_z}\, \mathrm{d}V,$$

$$\mathbf{Q} = \sum_i^n \int_{(e)_i} \mathbf{N^T}\, \dot{q}\, \mathbf{N} \mathrm{d}V.$$

Here, n is the number of elements and the subscript i refers to the individual finite element $(e)_i$, and **N** and ∇**N** represent its interpolation function vector and matrix of spatial

derivatives, ($\partial N_j/\partial x = N_{x,j}$), obtained from each element, respectively:

$$\mathbf{N} = [N_1, N_2 \ldots N_n] \quad \nabla\mathbf{N} = \begin{bmatrix} \mathbf{N_x} = N_{x,j} \ldots N_{x,n} \\ \mathbf{N_y} = N_{x,j} \ldots N_{y,n} \\ \mathbf{N_z} = N_{x,j} \ldots N_{z,n} \end{bmatrix}.$$

The superscript **T** refers to the transpose of the element interpolation function vector or matrix of spatial derivatives.

Equation 8 can be written as $\mathbf{A}\mathbf{p}_{t+\Delta t} = \mathbf{b}$. The left-hand side of Eq. 8 is accumulated into the finite-element solution matrix, **A**, and the right-hand side into the vector, **b**. In order to find a unique solution of (8), the fluid pressure must be prescribed at least at one node in the computational domain. Well-related in- or outfluxes, $\mathbf{F_b}$, are included as nodal point sources or sinks (see Huyakorn and Pinder 1987) or surface integrals over the area of inlet or outlet finite elements such as in wells

$$\mathbf{F}_b = \sum_i^{n_b} \mathbf{n}_i \cdot \mathbf{q_{b,i}} \int_{(e)_i} \mathbf{N^T}\,\mathbf{N}\,\mathrm{d}S. \tag{9}$$

n represents the normal to the outward facing surface element, and $\mathbf{q_{b,i}}$ is the volumetric flow across the boundary that truncates the finite volume i.

2.3.2 *Finite-Volume Discretisation of the Transport Equation*

The transport equation (4) is discretised using a finite-volume scheme. As outlined above, this yields surface integrals over the finite-volume facets and volume integrals over the finite-volume sectors, the latter contributing to distributed sources and sinks. These integrals are indicated as (fv) and are defined in terms of the piecewise constant finite-volume interpolation functions M_j. For each finite element, there are as many sectors and facets contributing to corresponding node-centred finite volumes as there are nodes and connections between nodes in the finite element, cf. Huber and Helmig (2000). These constitute the finite element's finite-volume stencil for accumulation into a second solution matrix **A** and right-hand vector **b** used for the implicit or semi-implicit solution of the finite volume equations. For a first-order accurate upwind scheme, these integrals are

$$\phi_j \int_{(fv)_j} \mathbf{M}_j \frac{\partial \bar{c_j}}{\partial t}\,\mathrm{d}V + \underbrace{\int_{(fv)_j} \mathbf{n}\cdot\mathbf{v}\,\bar{c_c}\,\mathrm{d}S}_{\text{incoming advective flux}} + \underbrace{\int_{(fv)_j} \mathbf{n}\cdot\mathbf{v}\,\bar{c_u}\,\mathrm{d}S}_{\text{outgoing advective flux}}$$
$$+ \underbrace{\int_{(fv)_j} \mathbf{n}\cdot\mathbf{J}_{\text{disp, in}}\,\mathrm{d}S}_{\text{incoming dispersive flux}} + \underbrace{\int_{(fv)_j} \mathbf{n}\cdot\mathbf{J}_{\text{disp, out}}\,\mathrm{d}S}_{\text{outgoing dispersive flux}} - \int_{(fv)_j} \mathbf{M}_j\, q\,\mathrm{d}V = 0. \tag{10}$$

Subscripts u, c and d refer to the far-field upstream, current and downstream finite volumes (Fig. 4). Importantly, ϕ_j, the porosity of the finite volume j, is a composite of that of the contributing sectors across which it may vary when they belong to different finite elements.

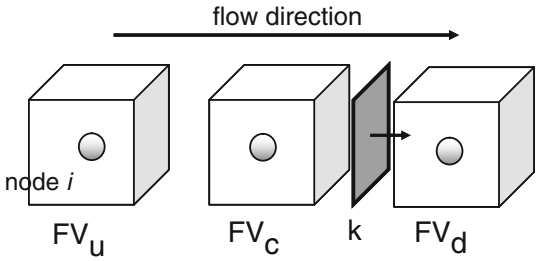

Fig. 4 Labelling convention for the spatial ordering of finite volumes with respect to the flow direction (in this case node-centred FVs matching hexahedral elements). Facet computations are always described with regard to the finite-volume facet, k, forming the boundary between the current (c) and the downstream finite volumes (d). This convention also applies to finite volumes located at an inflow or outflow model boundary

2.3.3 Time Discretisation of the Transport Equation

By discretizing the time differentiation in Eq. 10, the transport equation is again transformed into an algebraic equation of the shape $\mathbf{A}\bar{\mathbf{c}} = \mathbf{b}$. In the following discussion of this time discretisation, the dispersive flux will be neglected, but it will be considered in the next subsection.

In the explicit solution of this transport equation (cf., IMPES schemes, Durlofsky 1993; Huber and Helmig 1999), surface-integrated influxes multiplied with upwind concentrations and outfluxes multiplied with the concentrations of the current finite-volume cell are accumulated directly into the solution vector $\mathbf{x}$ initialised with products of the pore-volume and the concentration from the last time step

$$\mathbf{x}_j = \phi_j V_j - \triangle t \left[\sum_{k=1}^{f} H_{j,k} A_{j,k} \mathbf{n}_{j,k} \cdot \mathbf{v}\, \bar{c_u} + \sum_{k=1}^{f} (1 - H_{j,k}) A_{j,k} \mathbf{n}_{j,k} \cdot \mathbf{v}\, \bar{c_c} \right]$$
$$H_{j,k} = \begin{cases} 1 & \text{if } \mathbf{n} \cdot \mathbf{v} < 0 \\ 0 & \text{otherwise.} \end{cases} \tag{11}$$

Here $A_{j,k}$ and f denote the surface area of the finite-volume facet k and the number of facets per finite volume cell. H is the Heaviside function. Incoming fluxes are negative, since the normal is outward pointing. In the explicit formulation, the time increment, $\triangle t$, has to be so small that the total influx or outflux does not exceed the cell volume. This constitutes the problematic CFL constraint:

$$\triangle t \leq \frac{\phi_j V_j}{\max(F_{\text{incoming}}, F_{\text{outgoing}})}. \tag{12}$$

It is especially problematic in simulation models with variable finite volume size and/or permeability because small cells contributing to finite elements with a high permeability and/or low porosity often attract many order of magnitude greater fluid fluxes than the majority of cells. In explicit calculations, such models are subject to such a tight CFL global minimum that a prohibitive number of time increments becomes necessary to compute tracer breakthrough. CFL is dominated by a single or a volumetrically insignificant fast-flowing and/or highly adaptively refined fraction of the model.

In order to avoid the CFL restriction, we use an implicit approach. Time integration is performed by accumulating integrated facet-normal fluxes into the solution matrix, **A**. Its diagonal is initialised with the pore volume of the finite-volume cells divided by the arbitrarily large time increment

$$\mathbf{A}_{j,j} = \frac{\phi V_j}{\triangle t} + \sum_{k=1}^{f} (1 - H_{j,k}) A_{j,k} \mathbf{n}_{j,k} \cdot \mathbf{v} \tag{13}$$

$$\mathbf{A}_{j,i} = \begin{cases} \sum_{k=1}^{f} H_{j,k} A_{j,k} \mathbf{n}_{j,k} \cdot \mathbf{v} & \text{if cells } i \text{ and } j \text{ share the facets } k \\ 0 & \text{otherwise} \end{cases} \tag{14}$$

$$\mathbf{b}_j = \frac{\phi V_j}{\triangle t} \bar{c}_j^t + \bar{q}^{t+\triangle t}. \tag{15}$$

Upwinding is achieved by discriminating incoming fluxes as off-diagonal couplings, while outgoing fluxes are decoupled by accumulation into the matrix diagonal. This distinctive treatment is accomplished by the Heaviside function in Eq. 13. The right-hand vector, **b**, contains products of the pore volume and the current concentration divided by the time increment as well as the source and sink terms. The resulting sparse, positive definite, but asymmetric system of linear algebraic equations is solved using the algebraic multigrid method for systems (SAMG, Ruge and Stüben 1987; Stüben 1999).

Since finite volumes are truncated by model boundaries, the surface integration of fluxes over these cells cannot be used to evaluate the local divergence of the flow. Their flux sums will be negative where outflow and positive where inflow occurs. In order to close the domain integral, the corresponding terms must be subtracted from the diagonal of **A** or, if this would make it negative, added to **b**

$$\mathbf{A}_{j,j} = \mathbf{A}_{j,j} - \sum_{k=1}^{f} A_{j,k} \mathbf{n}_{j,k} \cdot \mathbf{v} \quad \text{if} \sum_{k=1}^{f} A_{j,k} \mathbf{n}_{j,k} \cdot \mathbf{v} < 0 \tag{16}$$

$$\mathbf{b}_j = \mathbf{b}_j + \bar{c}_j \sum_{k=1}^{f} A_{j,k} \mathbf{n}_{j,k} \cdot \mathbf{v} \quad \text{if} \sum_{k=1}^{f} A_{j,k} \mathbf{n}_{j,k} \cdot \mathbf{v} > 0. \tag{17}$$

2.4 Treatment of Diffusion

Physically meaningful diffusion can be re-introduced as a supplementary diffusive facet-normal flux, $\mathbf{J}_{\text{disp}}$

$$\mathbf{J}_{\text{disp}} = \int D_n \frac{\partial c}{\partial \mathbf{n}} \, \mathrm{d}S, \tag{18}$$

where $D_n = |\mathbf{n} \cdot \mathbf{D}|$ is the magnitude of the dispersion coefficient in the direction of the normal to the surface facet of the finite volume. However, the FVM method is inferior to the FEM with regard to the modelling of diffusive processes, and the treatment of the model boundaries becomes more complicated. Therefore, in any implicit solution procedure, we model diffusion with the FEM, accumulating corresponding element integrals directly into the system of linear algebraic equations that arises from the hyperbolic part of the transport equations. This is also our preferred way of treating compressible flow where CFL can no longer be calculated, cf. LeVeque (1987).

2.4.1 Higher Order-Accurate Solution Procedure

The implicit transport scheme (13) is superior to its explicit counterpart because arbitrarily large time steps are possible if the velocity field is constant, i.e. not affected by the advection of the concentration profile. For the advection of a passive solute, however, the first-order

scheme fails to preserve sharp concentration fronts, since the transport equation has a strongly hyperbolic character, e.g. Gudonov (1959), but the scheme is highly diffusive. This makes it desirable to extend the scheme to obtain higher-order accuracy.

The higher-order accurate simulation of the mass-conservative transport of a scalar property (known as the Riemann problem) is a lively area of research, and many robust schemes are available for regular grids, at least for one and two-dimensional models (LeVeque 1982, 1987). In order to make a transport scheme second-order accurate in space, one typically calculates an estimate of the gradient of the transported variable for each control volume. This approximation is non-trivial to obtain an unstructured grid with multiple material domains and is used in conjunction with the upwind cell values from the first-order scheme to improve the spatial integration. In order to suppress spurious oscillations that occur when the gradient of the transported variable is overestimated, it is a common practice to apply slope limiters that guarantee that the transport scheme becomes total variation diminishing (TVD). Limiting is phased in gradually, not to convert, for instance, *sin* waves into rectangular waves. Related to this is the issue of extrema detection in the transport variable field (Pain et al. 2003).

Our approach to this non-trivial task is outlined in the following. We introduce additional temporal limiting, hereafter referred to as Θ-limiting, cf. Pain et al. (2003). We will show that this extension permits a second-order accurate discretisation of time.

First, we use the finite-element basis functions to interpolate $\hat{c}$ from the finite-element nodes to the facet integration points k on the finite-volume facets to calculate the advective fluxes

$$\tilde{c}_k = \sum_{j=1}^{n} \mathbf{N}_j(k)\, \hat{c}_j. \tag{19}$$

Since transport is modelled in the finite-volume framework, the projection of $\bar{c}$ to $\hat{c}$ (Eqs. 6, 7) must precede the interpolations to the integration points of the facets. In practice, this helps to preserve sharp concentration gradients, but its most beneficial effect is to reduce discretisation effects in model regions where cell size varies or cells have a large aspect ratio.

Second, gradient estimates are assessed using the normalised variable approach, see Fig. 5. This procedure requires an estimate of the upstream value of c, referred to as $\bar{c}_u$. This value can be bracketed in terms of the minimum and maximum values of $\bar{c}$ at the finite-element nodes connected to the node on the upstream side of the finite-volume facet and excluding the downstream node, i.e. value $\bar{c}_d$. We estimate $\bar{c}_u$ from these bounds $\bar{c}_{\min}, \bar{c}_{\max}$

$$\bar{c}_u = \begin{cases} \bar{c}_{\max} & \text{if } \bar{c}_d \le \bar{c}_c \\ \bar{c}_{\min} & \text{if } \bar{c}_d > \bar{c}_c \end{cases}. \tag{20}$$

Now we can compare the variation of $\bar{c}$ from the upstream to the downstream finite volume and obtain for the current volume and the facet

$$U_c = \frac{\bar{c}_c - \bar{c}_u}{\bar{c}_d - \bar{c}_u}, \tag{21}$$

$$U_k = \frac{\tilde{c}_k - \bar{c}_u}{\bar{c}_d - \bar{c}_u}. \tag{22}$$

An overestimation of the gradient can be avoided by limiting U_k so that its value lies in the black area of Fig. 5

$$\tilde{U}_k = \begin{cases} \min\left(\xi\, U_c, 1, \max(0, U_k)\right) & \text{if } U_c \in [0, 1] \\ U_c & \text{otherwise} \end{cases}. \tag{23}$$

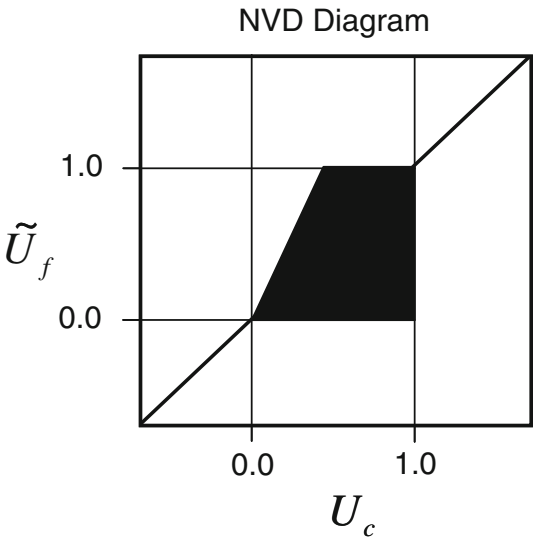

Fig. 5 Normalised variable diagram relating a transported variable value interpolated between two finite-element nodes separated by a FV cell boundary (*horizontal axis*), to its slope limited value at this interface (*vertical axis*). The black central area delineates the field of potential relations which will lead to oscillation-free TVD behaviour. (Unlimited) values outside this box will result in spurious oscillations

Variable ξ is an adjustable parameter. For ξ equal to 2, the limiting has the interesting property that in the presence of extrema, the scheme reduces to the first-order upwind solution, but moves smoothly between this and the second-order approximation of $\tilde{c}_k$ elsewhere

$$\tilde{c}_k = \tilde{U}_k \left(\bar{c}_d - \bar{c}_u\right) + \bar{c}_u. \tag{24}$$

We have experimented with the parameter ξ in Eq. 23 and results show that for values of 4–8, local point or saw-tooth extrema are advected with an impressively constant peak height; however, the scheme is no longer guaranteed to be TVD.

Third, we apply a central difference method to evolve the solution with time because this leads to an exact front position and second-order accuracy (Nessyahu and Tadmor 1988; Jiang and Tadmor 1998). However, for time steps on the order of the grid Courant number and above, this approach can result in numerical oscillations. In order to avoid this, we introduce the parameter Θ set to 0.5 for central and 1.0 for backward time differencing. The finite volume integrals for the second-order accurate time discretisation including the diffusive flux, $\mathbf{J}_d$, now take the form:

$$\begin{aligned}
&\phi_j \int_j^{(fv)} \left(\frac{\bar{c}_j^{n+1} - \bar{c}_j^n}{\triangle t} - \bar{q}_j \right) \mathrm{d}V \\
&= \int_j^{(fv)} \Theta \left(\mathbf{n} \cdot \mathbf{v}\, \hat{c}^{n+1} + D\, \mathbf{n} \cdot \nabla \hat{c}^{n+1} \right) \mathrm{d}S \\
&+ \int_j^{(fv)} (1 - \Theta) \left(\mathbf{n} \cdot \mathbf{v}\, \hat{c}^{n} + D\, \mathbf{n} \cdot \nabla \hat{c}^{n} \right) \mathrm{d}S.
\end{aligned} \tag{25}$$

For each time step and finite-volume facet, a value of Θ is calculated to satisfy the TVD criteria. Since the backward Euler time differencing is TVD, the same way as the first-order

upwind scheme, spatially, the Θ-corrected central difference scheme is guaranteed to be TVD as Θ approaches 1. The overall system of algebraic equations is solvable under the proviso that the diagonal of the solution matrix remains positive. This extra constraint is taken into account when Θ is calculated. We achieve this by measuring the temporal change in both upstream and downstream facet fluxes, and increase Θ gradually from 0.5 to 1.0 (Backward-Euler) as the local CFL limit is approached

$$
\begin{aligned}
g_k^{n+\frac{1}{2}} &= \int \left(\mathbf{n}_k \cdot \mathbf{v}^n\, \hat{c}^n + D\, \mathbf{n}_k \cdot \nabla \hat{c}^n\right) \mathrm{d}S - \int \left(\mathbf{n}_k \cdot \mathbf{v}^{n+1}\, \hat{c}^{n+1} + D\, \mathbf{n}_k \cdot \nabla \hat{c}^{n+1}\right) \mathrm{d}S, \\
\varphi_c^{n+\frac{1}{2}} &= \frac{\left(\bar{c}_c^{n+1} - \bar{c}_c^n\right) V_c}{g_k^{n+\frac{1}{2}}\, \triangle t}, \\
\varphi_d^{n+\frac{1}{2}} &= \frac{\left(\bar{c}_d^{n+1} - \bar{c}_d^n\right) V_d}{g_k^{n+\frac{1}{2}}\, \triangle t}, \\
\Theta_k^{n+\frac{1}{2}} &= \max\left\{\frac{1}{2}, 1 - \Omega\, \min\left\{\left|\varphi_c^{n+\frac{1}{2}}\right|, \left|\varphi_d^{n+\frac{1}{2}}\right|\right\}\right\},
\end{aligned}
\tag{26}
$$

where Ω is a weighting term that is discussed further below. The diagonal of the solution matrix can still become negative if the flow field strongly converges around a sink or if poro-elasticity dominates flow transients and $\bar{q}_j$ in Eq. 25 dominates. In this case, we make a part of $\bar{q}_j$ explicit by shifting it from **A** to **b**. In order to calculate the desirable shift, we first evaluate the time-averaged divergence of flow in finite volume j for the current time step

$$
\sigma_j = \frac{1}{2}\left(\int_{(fv)_j} \mathbf{n} \cdot \mathbf{v}^{n+1}\, \mathrm{d}S + \int_{(fv)_j} \mathbf{n} \cdot \mathbf{v}^n\, \mathrm{d}S\right) / \left(\phi_j V_j\right). \tag{27}
$$

This estimate then allows to define Ω_j (Fig. 6), and distribute $\bar{q}_j$ between the matrix and the right-hand vector:

$$
\Omega_j = \frac{\sigma_j \triangle t - 1 + \mathrm{e}^{-\triangle t\, \sigma_j}}{\sigma_j \triangle t \left[1 + \mathrm{e}^{-\triangle t\, \sigma_j}\right]}. \tag{28}
$$

In order to use Ω-weighting in the Θ-limited central difference approach, its values should always be greater than $\frac{1}{2}$:

$$
\Omega_j = \max\left[0.5, \frac{\sigma_j^{n+\frac{1}{2}} \triangle t - 1 + \mathrm{e}^{-\triangle t\, \sigma_j^{n+\frac{1}{2}}}}{\sigma_j^{n+\frac{1}{2}} \triangle t \left[1 + \mathrm{e}^{-\triangle t\, \sigma_j^{n+\frac{1}{2}}}\right]}\right]. \tag{29}
$$

The Ω-weighting guarantees that transient sources or sinks can be taken into account appropriately. Its application whenever the divergence of the flow field is non-zero makes our new transport algorithm very stable, even in the presence of rapidly changing flow fields. This implies that the higher-order accurate transport scheme can be applied to a fully transient pressure regime.

In the higher-order finite-volume discretisation of the transport equation, the flux-limited finite-element approximation $\tilde{c}$ replaces the first-order upwind approximation $\bar{c_u}$ (Eq. 13) and the source $\bar{q}_j$ also includes all local flow-field related divergence terms. Due to the

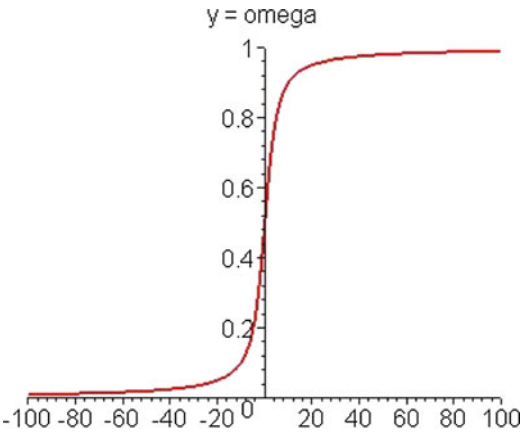

Fig. 6 Weighting function Ω for divergence of flow field. Through multiplication with Ω, implicit positive divergence contributions, arising at the time level $t + 1$ which would normally be subtracted from the diagonal of the solution matrix, are made explicit, by moving them to the right-hand vector

flux-limiting, this equation is now non-linear and needs to transformed into a linear system of equations before it can be solved. We achieve this by means of a Picard iteration in which the first-order upwind solution serves as an initial guess of $\bar{c}^{t+\Delta t}$ at the iteration level $p + 1$. The solution is iteratively improved until changes between iteration levels $\triangle \bar{c}^{p+1} = \left| \left(\bar{c}^{t+\Delta t}\right)^{p+1} - \left(\bar{c}^{t+\Delta t}\right)^{p} \right|$ diminish below a specified tolerance ϵ.

Including Θ-limiting and Ω-weighting, the full spatially and temporarily limited higher-order iteration scheme becomes

$$
\begin{aligned}
&\phi_j \int\limits_{(fv)_j} M_j \frac{\partial \bar{c_j}^{p+1}}{\partial t}\, \mathrm{d}V \\
&\quad + \int\limits_{j,\text{incoming}}^{(fv)} \mathbf{n}\cdot\mathbf{u} \left(\bar{c_u}^{t+\Delta t}\right)^{p+1} \mathrm{d}S + \int\limits_{j,\text{outgoing}}^{(fv)} \mathbf{n}\cdot\mathbf{u} \left(\bar{c_c}^{t+\Delta t}\right)^{p+1} \mathrm{d}S \\
&\quad + \Theta \int\limits_{(fv)_j} \mathbf{n}\cdot\mathbf{u} \left(\tilde{c}^{t+\Delta t}\right)^{p} \mathrm{d}S + (1-\Theta) \int\limits_{(fv)_j} \mathbf{n}\cdot\mathbf{u} \left(\tilde{c}^{t}\right)^{p} \mathrm{d}S \\
&\quad - \int\limits_{j,\text{incoming}}^{(fv)} \mathbf{n}\cdot\mathbf{u} \left(\bar{c_u}^{t}\right)^{p} \mathrm{d}S - \int\limits_{j,\text{outgoing}}^{(fv)} \mathbf{n}\cdot\mathbf{u} \left(\bar{c_c}^{t}\right)^{p} \mathrm{d}S \\
&\quad - \Omega_j \int\limits_{(fv)_j} M_j \left(q_j^{t+\Delta t}\right)^{p} \mathrm{d}V - (1-\Omega_j) \int\limits_{(fv)_j} M_j \left(q_j^{t}\right)^{p} \mathrm{d}V = 0.
\end{aligned}
\tag{30}
$$

It needs to be stressed that while the presented pressure-concentration formulation is for slightly compressible fluids only, the outlined approach is completely general. It can also be applied to compressible multiphase flow.

We have found that simultaneous diffusion is best computed with the finite-element method. In order to integrate this into the transport scheme, the corresponding finite-element volume integral

$$
\mathbf{D}\nabla^2 c = \int_{\text{FEM}} (\nabla N)^T \mathbf{D} \nabla N \, dV \tag{31}
$$

is just accumulated into the same solution matrix!

Table 3 Material properties and initial conditions for discrete fracture models

Parameter	Units	CURVED	BED3	FRACS2000
X-dimension	m	100	18	1,000
Y-dimension	m	50	8	200
Z-dimension	m	100	NA	1,000
Matrix pore volume	m^3	NA	36.6	5×10^7
Fracture volume	m^3	9.9	0.57	4,658
Fracture surface area	m^2	9,901	1.86	6,132,890
Specific A_f	$m^2\ m^{-3}$	0.02	0.05	0.03
Aperture range	m	0.001	0.0001–0.0012	0.0005–0.0035
Porosity	X	0.25	0.25	0.25
q_f/q_m		NA	152×10^3 / 25.8	83.3 / 0.3
log k_m	m^2	−12	−14 / −10	−14 / −10
Mesh properties				
Nodes		5,670	44,911	223,705
Elements		10,899	69,652	1,113,580

Parameter q_f/q_m is the fracture–matrix flux ratio. Y points upward and Z to the front in a right-hand coordinate system. Finite element area or volume in individual models varies by 2–5 orders of magnitude

2.5 Models and Configuration of Numerical Experiments

Several models are used to evaluate the performance of the implemented scheme, see Table 3. First, the schemes' performance is illustrated with simple conceptual fracture–matrix models. Then, the numerical dispersion incurred at different time-step sizes is measured and contrasted with the macro-dispersivity of two field data-based DFM models that are described in the following.

2.5.1 Layered Fractured Carbonate Model BED3

The 2D DFM model (Fig. 7; Table 3) is based on a map of a layer in an analogue carbonate reservoir in the Bristol Channel Basin, UK (Belayneh et al. (2006)). Fracture aperture varies between 0.1 and 1.2 mm as a function of fracture length. We have discretised this model with a commercial finite-element mesh generator,[1] representing the fractures with lower dimensional line elements. This resolves the computational problems posed by fracture elements with very large aspect ratios, see Juanes et al. (2002) and Paluszny et al. (2007).

The model is initially saturated with pure water, then a fluid with the same density and viscosity but different tracer concentration, $c = 1\,\mathrm{kg/m^3}$, is injected continuously through the left boundary. A pressure differential of 10^3 Pa is applied between the left and right constant pressure boundaries. Simulations are carried out for two different fracture–matrix flux ratios, cf. Matthäi et al. (2007a), of 25.8 and 152×10^3, respectively. The fracture–matrix flux ratio measures the importance of the fractures for the total flow through a block relative to the rock matrix. Its calculation involves that of the matrix flux, q_m, computed from the applied far-field fluid pressure gradient, ∇p, in the direction of flow such that $q_m = (V_m/(V_f + V_m))(k_m/\mu)A\nabla p$, where V_m and V_f are the matrix and fracture volumes,

[1] ANSYS ICEMCFD Tetra mesher operated in surface mode.

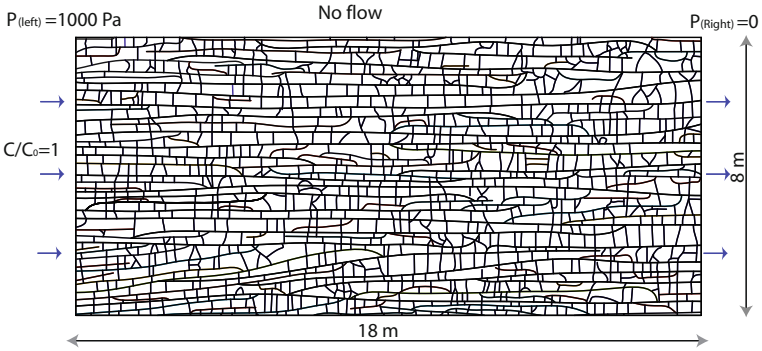

Fig. 7 Model of fractured limestone bed in plan view (BED3 of Belayneh et al. 2006). The model contains three sets of intersecting fractures formed sequentially during the prolonged deformation history of the sedimentary sequence

A is the cross-sectional area of the model perpendicular to the direction of flow. Keeping the original fracture permeability range constant, this is achieved by reducing the uniform permeability of the rock matrix from 10^{-10} to $10^{-14}\,\mathrm{m}^2$. Obviously, the first matrix permeability value is unrealistically high, but it is used for illustrative purposes. The fracture–matrix flux ratio, $q_\mathrm{f}/q_\mathrm{m}$, is calculated from the block-scale Darcy volume flux, q_t, so that $q_\mathrm{f}/q_\mathrm{m} = (q_\mathrm{t} - q_\mathrm{m})/q_\mathrm{m}$.

2.5.2 Disc-Shaped Fracture Model FRACS2000

The 3D DFM model, FRACS2000 (Fig. 8; Table 3), was stochastically generated by Paul LaPointe, and its properties are described in detail in Matthäi et al. (2007a). Model FRACS-2000 contains two sets of fractures observed in a US onshore oil field in the San Andreas formation, CA, USA. The fracture diameter distribution in each set is log normal and the fracture aperture varies between 0.1 and 3.5 mm. This distribution was created by correlating aperture with fracture diameter taking into account borehole data and observations on

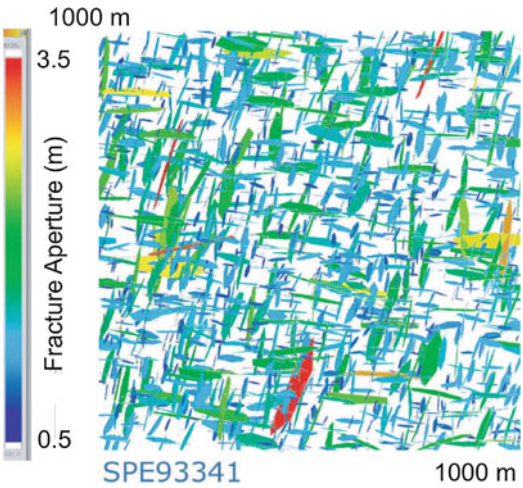

Fig. 8 Stochastic discrete fracture model FRACS2000 with two approximately orthogonal sets containing 1,000 disc-shaped fractures each, with a log-normal diameter distribution. Model was created with the FRED software by P. LaPointe (Golder Assoc. Inc.), and is documented in Matthäi et al. (2007a)

drillcore. The model has a size of 1,000 × 1,000 × 200 m and contains 2,000 fractures. Lower dimensional surface elements represent the fracture, and in total, the model is discretised with 1,113,580 hybrid elements, cf. Paluszny et al. (2007). Model FRACS2000 is unique in terms of its complexity, level of detail and size. A pressure differential of 5 MPa is applied between the opposing left and right boundaries and no flow conditions are set at all the other boundaries. Similar to model BED3, runs were conducted with two different permeabilities of the rock matrix, 10 mD and 100 D. Again the latter value is unrealistically high and was chosen only to evaluate numerical dispersion at a very low fracture matrix flux ratio.

Initial and boundary conditions for model FRACS2000 are the same as for model BED3. A hydrostatic fluid pressure far-field gradient resulted from the applied fluid pressure differential.

2.6 Macro-Dispersivity

Spatial and temporal moments derived from stochastic theory for solute transport in heterogeneous domains can be used to define macroscopic or upscaled parameters. The macro-dispersion tensor is the dispersion tensor needed in calculations with uniform coefficients to meet the same second-central moments as the ensemble-averaged concentration in a heterogeneous domain. The zeroth moment , μ_0, first moment, μ_1, second moment, μ_2, mean, $\bar{X}$ and variance, σ, are defined by

$$\begin{aligned}
\mu_0 &= \int_0^L c(x)\mathrm{d}x \\
\mu_1 &= \int_0^L c(x)x\mathrm{d}x \\
\mu_2 &= \int_0^L c(x)x^2\mathrm{d}x \\
\bar{X}(t) &= \frac{\mu_1}{\mu_0} \\
\sigma(t) &= \frac{\mu_2}{\mu_0} - \left(\frac{\mu_1}{\mu_0}\right)^2 .
\end{aligned} \tag{32}$$

In order to evaluate the numerical dispersion associated with the IMP–IMS numerical scheme, the macro-dispersion, $D(t)$ and macro-dispersivity, $\alpha(t)$, were used, calculated as follows

$$\begin{aligned}
D(t) &= \frac{\mathrm{d}\sigma(t)}{2\mathrm{d}t} \\
\alpha(t) &= \frac{\mathrm{d}\sigma(t)}{2\mathrm{d}\bar{X}(t)}.
\end{aligned} \tag{33}$$

2.7 Averaging Concentration

In order to compare the results of different simulations, we compute concentration profiles in the direction of the far-field fluid pressure gradient, averaging concentration on planes perpendicular to this transport direction. These averages are non-trivial to obtain, given the

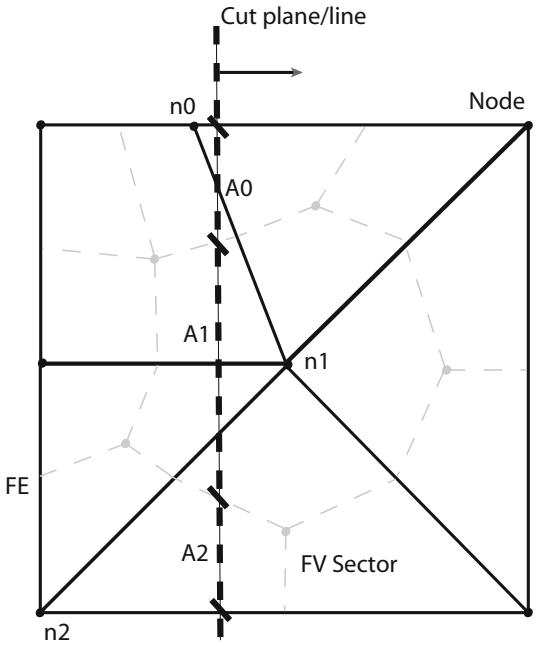

Fig. 9 Cut plane (*line*) dissecting two dimensional FV-FE stencil so that a new surface (*line segment*) is created. In two dimensions, a pair of newly generated points delimited the intersection between the line and the finite volume cell: [(n0,A0),(n1,A1),(n2, A2)]. Summing the normalised line length-concentration products, the one-dimensional concentration average is calculated, see Eq. 34

unstructured mesh and the lower-dimensional representation of the fractures. We construct cut planes through the virtual finite-volume mesh (cf., Paluszny et al. 2007), computing their intersection with each finite-volume sector (Fig. 9). In order to obtain the average concentration on a cut plane, sector area-concentration products are accumulated, and the result is normalised by the cut plane total area. Note that the transport variable has a constant value in each finite volume and therefore also in any one of its sectors. This reflects the piecewise constant finite volume interpolation functions, M:

$$\overline{c} = \frac{\sum_{i=0}^{\text{Nodes}} M_i c_i A_i}{\sum_{i=0}^{\text{Nodes}} A_i}, \tag{34}$$

where A_i denotes the area of the cut plane/line–FV sector intersection, and c_i is the concentration value in the finite volume i.

3 Results

Here, we first establish the IMP–IMS scheme's characteristics in one dimension; then, we examine its geometric flexibility with surfaces and large-aspect ratio volumes in space, considering the passive advection of solutes in fractured rock. The result section concludes with the analysis of the numerical dispersion incurred at different levels of CFL overstepping and a comparison with the physically meaningful macro-dispersion due to the presence of the fractures. Some recommendations are made regarding the recommended degree of CFL overstepping.

Pure advection simulations for a one-dimensional step profile at increasing CFL numbers (Fig. 10) indicate that the scheme reaches the theoretical maximum accuracy for irregular meshes at CFL ≤ 0.1. At such small CFL numbers, the Picard iteration converges in a few cycles, the slope limiter is phased in only weakly and the theta-limiting achieves

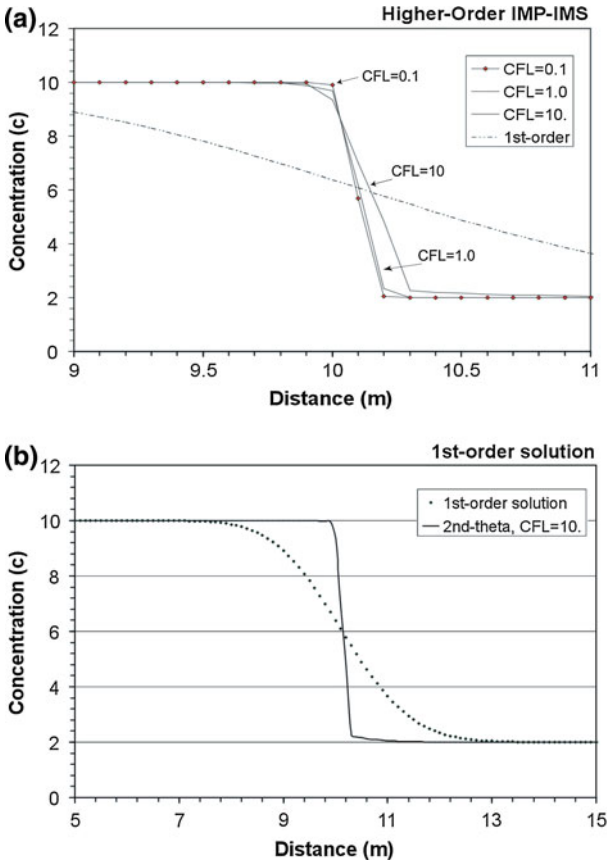

Fig. 10 Resolution of shock fronts by Θ-limited higher-order method as a function of grid Courant number. **a** Results of one-dimensional simulations for the advection of a step function for CFL = 0.1, 1.0 and 10. **b** Worst-case (equivalent to first-order solution) in comparison with CFL = 10 solution. First-order curve is for CFL = 10 and a very large transport distance to illustrate problem of numerical dispersion

higher-order accuracy in time in most of the model domain. At high values (CFL $\geq$ 1,000) in a homogeneous model, the second-order accuracy reduces to first-order accuracy as a consequence of the limiting. The front begins to lag by one half of a CFL step, but this is hard to verify since the front is diffuse at such high CFL values. Also, depending on the set tolerance, ϵ, the Picard iteration may take more than 100 cycles to converge. An early termination of the iteration loop may lead to mild oscillations near the front. The bijective mapping of the transport variable assumes a special role because it reduces the mesh dependency of the finite-element interpolation of concentrations onto the facet integration points. Without it, fronts will advance slightly faster in coarsely discretised regions as compared with more refined regions.

Figure 11 shows a tracer front in a contrived fracture surface geometry that includes geometrically challenging features such as small-angle fracture intersections, irregular boundaries and constrictions. Although the solution was computed for a global CFL value of 100, it is close to a CFL value of $\leq$1 over much of the fracture surface area. The more diffusive behaviour at large CFL in the fast-flowing subregions of this model is offset by their increased mesh refinement. While simulations at very large CFL numbers reveal a behaviour of the higher-order accurate transport scheme that is highly diffusive (Fig. 10b), the method still remains conservative and bounded.

As discussed in detail in Pain et al. (2001), the element aspect ratio is a key control on the discretisation error in finite-element models. The discretisation of fractures in model

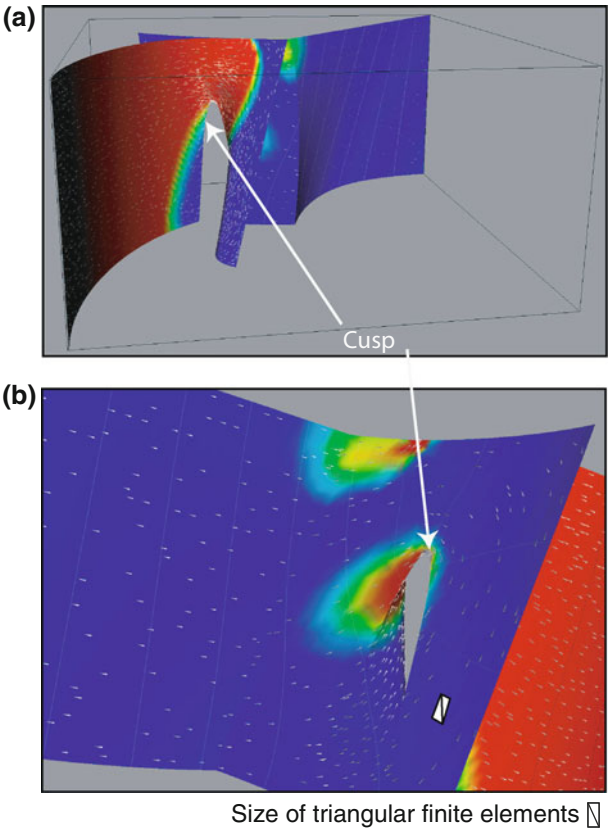

Fig. 11 Illustration of the higher-order accurate Θ-limited transport scheme at a global CFL number of 100. Concentration is shown in *rainbow shading* (*red* = 1, *blue* = 0). Model geometry (**a**) was chosen to include complicated boundary shapes and acute fracture intersections. Note the close to optimal representation of the sharp front near the cusp. **b** Subregion of model relating front width to finite-element size

PRISM1 with large-aspect ratio prism elements (≤150, see Fig. 12 of Paluszny et al. 2007) is feasible because fluid-pressure gradients along the fractures tend to be strongly reduced as fracture permeability typically is orders of magnitude greater than that of the rock matrix. The matrix surrounding fracture tips, however, have to be closely resolved because pressure gradients therein are high, see Paluszny et al. (2007).

When applied to strongly heterogeneous and adaptively refined discrete fracture models with very tight global CFL constraints (e.g. model FRACS2000, Table 3; Fig. 12), the new scheme reveals its genuine superiority relative to the IMPES method. As will be shown below, this advantageous behaviour characterises all our geometrically more complex simulations, and we have obtained high-quality results for overstepping of the global CFL number by up to a factor of 10,000. In the latter case, the scheme still operates at higher-order accuracy in large portions of typical fracture–matrix models (see results below). This applies because flow-velocity histograms for fractured rock masses (Matthäi and Belayneh 2004) indicate that while the fast-flowing volume fraction tends to constitutes less than 1% of the model volume, flow velocity in these regions often exceeds that in the rock matrix by more than

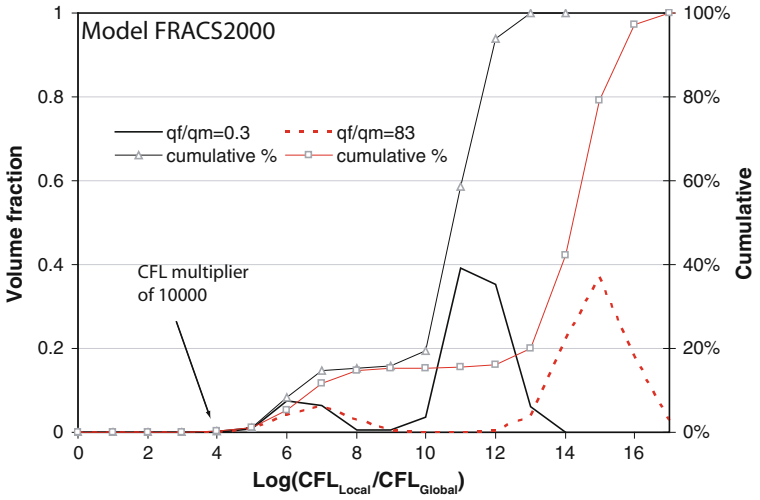

Fig. 12 Flow-volume weighted CFL histograms for the two different q_f/q_m realisations of the FRACS2000 model. *Horizontal axis* gives the decadic logarithm of the ratio between local FV cell CFL and the global CFL minimum value. For model realisation 1 ($q_f/q_m = 0.3$), the cumulative volume fraction curve shows that global CFL can be exceeded by above 10^6, before less than 10 vol% of the model is supercritical (CFL >1). For realisation 2 ($q_f/q_m = 83$) the cumulative volume fraction curve shows that global CFL can be exceeded by above 10^6, before more than 5 vol% of the model is supercritical (CFL >1)

three orders of magnitude. These characteristics are most beneficial for the application of the proposed IMP–IMS transport scheme.

3.1 Comparison of IMPES and IMP–IMS Formulations

The numerical dispersion incurred by the large step implicit scheme is evaluated through a comparison of the results with a second-order accurate IMPES scheme applied for very small global time steps. Having quantified the numerical dispersion by this approach, we compare it with the macro-dispersivity induced by the presence of the fractures. This permits to evaluate whether and above which time-step value the numerical dispersion becomes significant relative to the macro-dispersion in the fractured porous medium. A series of simulations is carried out with model BED3 to perform this evaluation. Four different schemes are employed to calculate solute transport in this 2D model with first-second-order and flexible accuracy. A CFL number of one is used to calculate the numerical disperson caused by the first-order accurate IMP–IMS schemes.

The concentration fronts computed with the second-order accurate IMPES scheme applied to model BED3 are shown in Fig. 13. For the high fracture–matrix flux ratio of 152,000 (Fig. 13a), tracer movement is restricted entirely to the fractures. Interestingly, some of the cross fractures oriented perpendicular to the far-field fluid pressure gradient are not utilised by the flow. For the low fracture–matrix flux ratio of 25.8 (Fig. 13b), significant tracer transport occurs through the rock matrix, leading to a smeared tracer distribution and a more gradual advance of the tracer front in the rock matrix reaching 3 m after 24 h.

Line-averaged concentration profiles for model BED3 are shown in Fig. 14. The results of IMPES and IMP–IMS first second order runs are nearly identical and essentially dispersion free, while the first-order accurate IMPES and IMP–IMS schemes introduce some numerical

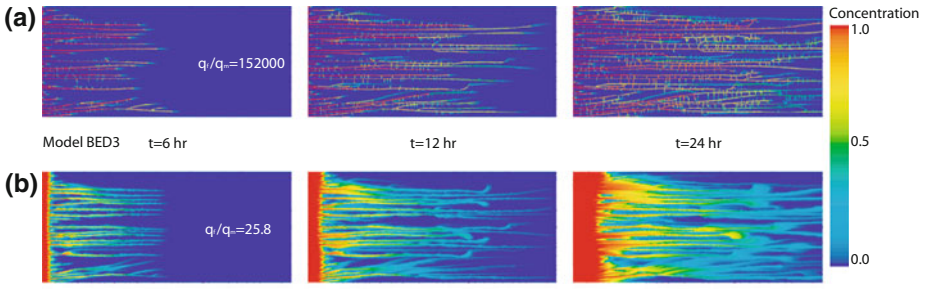

Fig. 13 Concentration fronts in model BED3 as computed with the second-order explicit scheme for different rock permeabilities, **a** $k_m = 10^{-14}$ m^2, **b** $k_m = 10^{-10}$ m^2

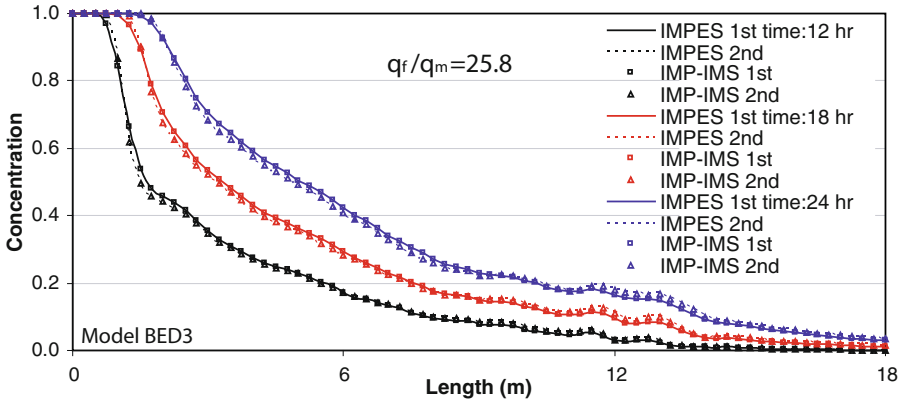

Fig. 14 Line-averaged concentration profiles in model BED3 as obtained with first- and second-order explicit (IMPES) and implicit/semi-implicit transport schemes

dispersion. In the following discussion, the results of the IMPES second-order scheme will be considered as reference solutions. The mechanical dispersion on the model scale is greater for the higher fracture–matrix permeability contrast than for the lower one Fig. 15. Its value is 1.01×10^{-3} m^2 s^{-1} for the fracture–matrix flux ratio of 152,000 and 4.04×10^{-4} m^2 s^{-1} for that of 25.8.

The effects of using different CFL multiplier are elucidated by comparison of corresponding results with the reference solutions. The macro-dispersion and macro-dispersivity of concentration results for second-order IMPES scheme and IMP–IMS scheme with different CFL multiplier are shown in Fig. 15. These result shows that using a CFL overstepping by a factor of 100 still gives accurate results for both cases. The L^2 error norm, is less than 0.5% for the macro-dispersivity values. Figure 16 shows the concentration distribution averaged along the flow direction. It can be seen that even the error caused when using a CFL multiplier of 1,000, is neglible for the model with the lower matrix permeability and small for that with the higher one. In all the conducted experiments, the error is larger before the solute breaks through the downstream model boundary than afterwards.

When we introduced CFL (Eq. 12) in Sect. 2.3.3, we observed that—often—a volumetrically insignificant fraction of highly refined fast-flowing finite-volume cells control global CFL. This applies exactly to DFM models. For models BED3 and FRACS2000, we can now quantify this critical fraction and relate it to the remainder of the cells model that stay

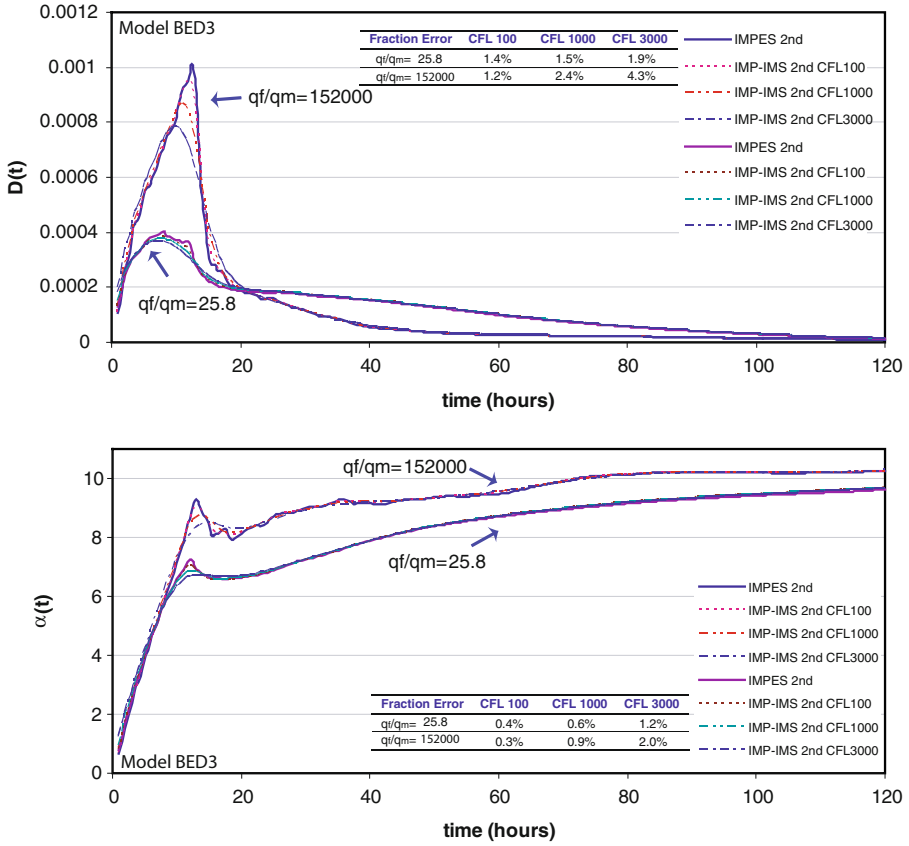

Fig. 15 Macro-dispersion and dispersivity as measured in model BED3 for implicit/semi-implicit schemes for different degrees of CFL overstepping. Average normalised errors were calculated from the macro-dispersion/dispersivity

subcritical for any given amount of global CFL overstepping. In the following, we use the supercritical volume fraction to formulate a new CFL-guided time-step selection method for implicit and semi-implicit transport simulations.

In order to find a selection criterion for the factor by which the CFL condition can be overstepped while retaining an acceptable mechanical- to numerical dispersion ratio, it is instructive to plot CFL values in flow-volume-weighted histograms (Figs. 12, 17). These plots illustrate the volume fraction of the model that is supercritical with regard to CFL for a given choice of global CFL overstepping and spatially adaptively refined FEM–FVM mesh. Thus, if we overstep global CFL by a factor of 100 in the model of BED3 with a $q_\mathrm{f}/q_\mathrm{m} = 152{,}000$, then about 80% of all the elements still have a CFL value below 1. Even if we overstep CFL by a greater factor of $\leq$10,000 for BED3 with a lesser $q_\mathrm{f}/q_\mathrm{m}$ ratio of 25.8, still more than 75% of all the elements remain sub-CFL. It follows that at high fracture matrix flux ratios, even single-step transport calculations are sufficient to calculate the statistical moments of the concentration distribution and macro-dispersivity with an overall error of $\leq$20%. Thus, individual model realisations can be analysed within minutes as opposed to

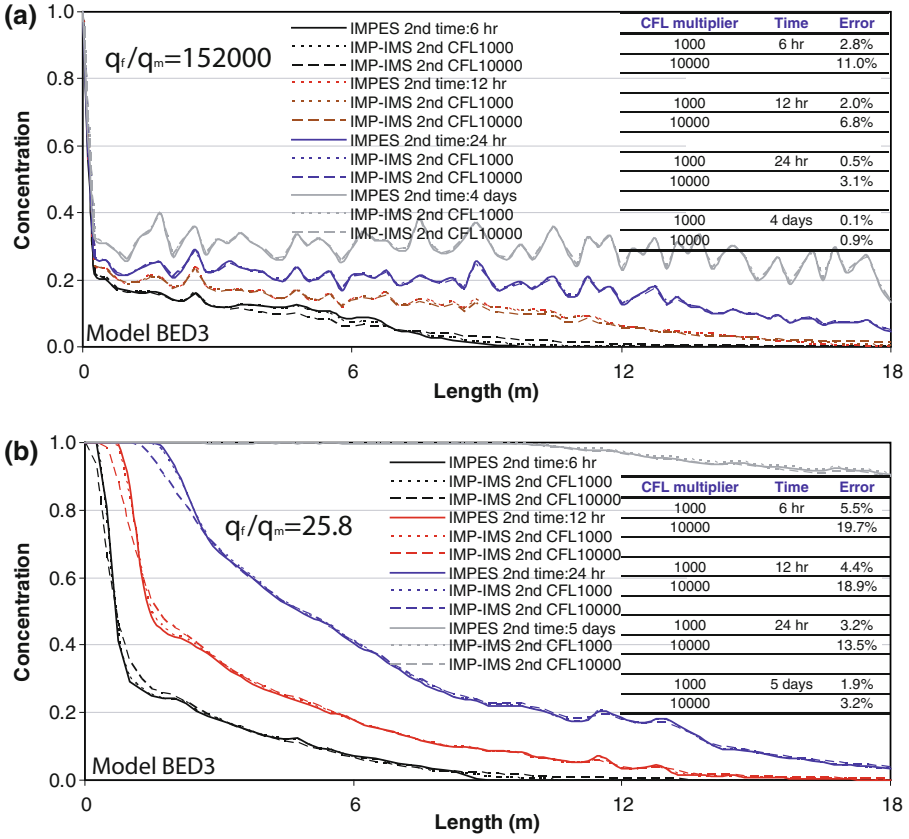

Fig. 16 Line-averaged concentration profiles in model BED3 for second-order explicit and implicit schemes. The errors, L^2 norms, are calculated for both the models

weeks required by the second-order IMPES scheme. This means that uncertainty can be analysed quickly and on a large number of model realisations.

For a large global CFL, the following key features of the implicit/semi-implicit transport scheme are apparent from the results obtained with model BED3:

- The discrepancy between the reference results and those obtained using CFL overstepping by a factor of 10,000, is negligible after breakthrough at least for model realisations with the higher fracture–matrix flux ratio.
- The IMP–IMS scheme gives reasonable results at a fraction of the computational cost of the second-order accurate IMPES scheme that was used to compute the reference solution.
- We observe enhanced numerical dispersion in experiments with a more permeable rock matrix.
- Using large time-step sizes only violates the Courant–Friedrich–Levy condition in small subvolumes of the model where the smallest control volumes coincide with the fast-flowing fractures.
- A high degree of CFL overstepping should be possible in stationary velocity systems. Thus, this approach appears ideally suited to model tracer experiments where density or

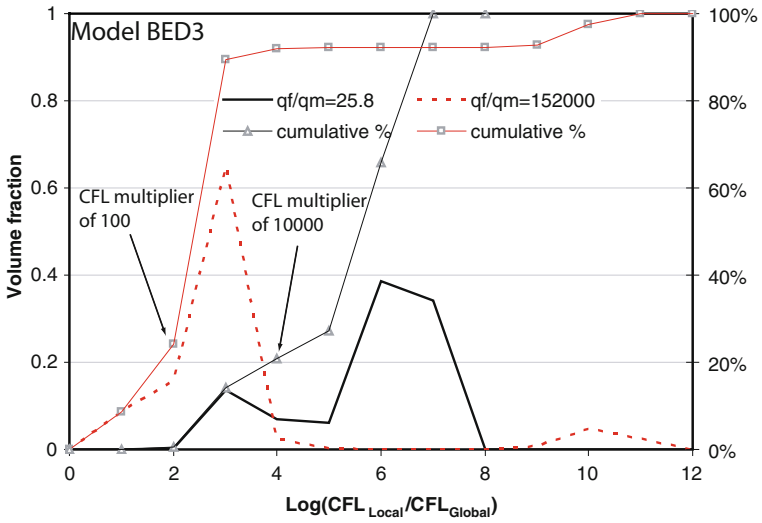

Fig. 17 Flow-volume weighted CFL histograms for model BED3 and the two different matrix permeabilities of 100 D and 10 mD, respectively

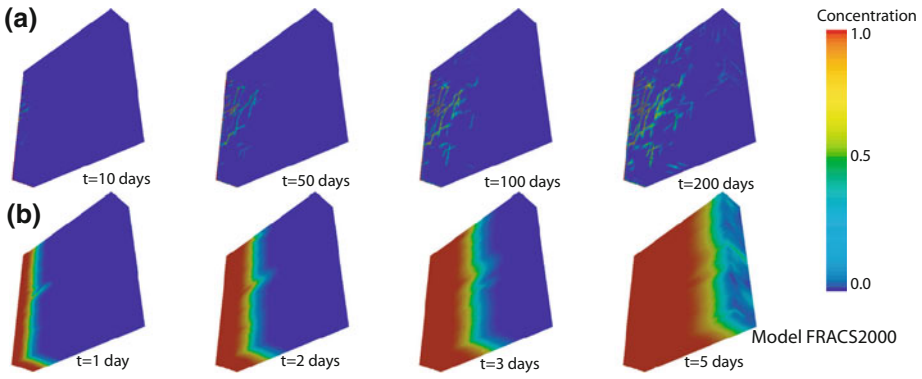

Fig. 18 Concentration fronts in model FRACS2000 as computed with the second-order implicit scheme for different rock permeabilities (FRACS2000). **a** Result for a global CFL multiplier of 1,000,000 and the lower matrix permeability of 10 mD, **b** result obtained for a CFL multiplier of 1,000 and the high matrix permeability of 100 D

viscosity changes as a function of concentration have no or little effect on the velocity field; else, the latter has to be updated frequently, cf. Nick et al. (2008).

Figures 12, 18 and 19 show the CFL histogram, the concentration front and the line-averaged concentration profiles computed with the 3D model FRACS2000 (Fig. 8). Due to the size and heterogeneity of this model, a second-order accurate IMPES simulation could not be obtained as a reference solution. In the computation of the concentration fronts (Fig. 18), CFL was overstepped by a factor of 10^6 for the model realisation with the 10 mD matrix permeability and fracture matrix flux ratio of 83.3, and by 10^3 for the realisation with the unrealistically high matrix permeability of 100 D and a correspondingly lower fracture–matrix flux ratio of 0.3. For the high fracture–matrix flux ratio (Fig. 18a), the tracer advances along a tortuous path, and high concentrations are largely restricted to the fractures and narrow rock

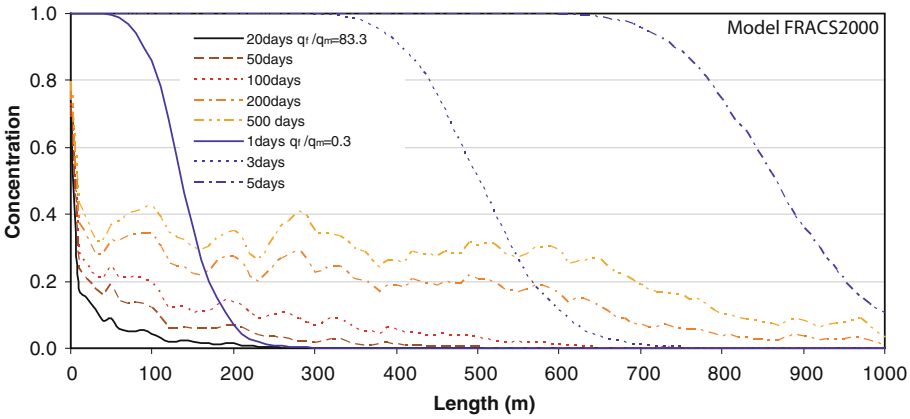

Fig. 19 Line-averaged concentration profiles in model FRACS2000 as computed with the second-order implicit scheme and the two different matrix permeabilities, i.e. $k_m = 10^{-10}, 10^{-14}$ m^2

bridges between them. A mere visual examination of these results already shows that the mechanical dispersion caused by the fractures dominates the numerical dispersion. Breakthrough occurs early (after 3 days) at a very small overall tracer concentration in the model (<5%). For the low fracture–matrix flux ratio, tracer advance is almost unaffected by the presence of the fractures (Fig. 18b), and a very diffuse front develops, similar to the one expected for a first-order accurate scheme applied to a homogeneous porous medium. This behaviour can be rationalised when considering the CFL histogram for this model (Fig. 12): For CFL overstepping by a factor of 1,000, the majority of finite-volume cells are supercritical (CFL >1). Dependent on the actual degree of overstepping in each of these cells, solution accuracy becomes first order in the worst case. On the other hand, the CFL range in this model is much smaller than in the one with the high fracture–matrix flux ratio, and it can therefore be computed more quickly potentially even with an IMPES scheme.

Similar to model BED3, the line-averaged tracer concentration profiles computed for model FRACS2000 (Fig. 19), show a long leading edge in the tracer front. This marks 'anomalous' (non-Fickean) transport (cf., Fig. 3, Berkowitz and Scher 1997). This behaviour cannot be modelled using the classical ADE approach relying on the concept of macro-dispersivity as expressed by a symmetric tensor (Cortis and Birkholzer 2008). However, the tracer profiles observed in models BED3 and FRACS2000 can be modelled using the Continuous-Time Random-Walk Method (CTRW, Berkowitz and Scher 1997; Cortis and Birkholzer 2008). The proposed scheme is well suited for the calculation of the parameters required by this approach.

Apart from the quantification of the numerical dispersion, the visualised tracer fronts also illustrate that the fracture networks in low permeability rocks govern the mixing of solutes. Solute entering the model at different positions at the upstream boundary is focused into individual fractures and dispersed again at their downstream termination. This process occurs repeatedly during flow through the models and is associated with repeated acceleration and deceleration of the flow. These high-flow velocity contrasts induced by spatially correlated permeability variations also foster solute mixing.

4 Discussion

Preliminary testing of our new higher-order accurate transport scheme on fractured reservoir models has produced a number of interesting results and insights: As the smallest elements are located at fracture intersections, the solution is more diffusive (at worst first-order accurate) only in these highly refined areas, but second-order accurate in space and in time anywhere else. However, when concentration is high enough to affect fluid density, concentration changes feedback into the large-scale velocity field. Now updating the velocity field often enough is crucial for correct prediction of transport and the position of advancing tracer fronts. Here, it appears to be better to invest computational resources into frequent updates of the velocity field than more costly higher-order solutions. How often the velocity-field needs to be updated, depends on model geometry, resolution, the ratio between viscous and gravitational forces and on the overall model heterogeneity.

Even if an implicit transport scheme is used, the CFL criterion appears as a useful guide for the choice of the global time step. We advocate a flow-volume percentage-based degree of CFL overstepping because the volume fraction of supercritical finite-volume cells is quasi-linearly related to the associated numerical dispersion. This choice is rationalised also when considering the effect of the dispersion on the tracer/solute plume as a whole. On the other hand, the numerical dispersion has a significant effect on the first arrival of the tracer and the definition of the tracer front in the fracture network. This effect is not appropriately addressed by the volumetric treatment proposed here.

A further gain in computation speed for large models ($>10^6$ FV cells) could be achieved through the application of the Adaptive Implicit Method (AIM, e.g. Thomas and Thurnau 1982) in conjunction with the proposed transport scheme. For a given choice of CFL overstepping, AIM computes sub-CFL cells explicitly, while super-CFL cells are assembled into a matrix equation and solved implicitly. The CPU time required for an explicit as compared with an implicit calculation is highly implementation dependent and varies with the scaling characteristics of the linear algebra solver of choice. For our particular C++ implementation combined with the algebraic multigrid solver for systems (SAMG) applied to the FRACS2000 model, a single implicit transport step (largely irrespective of step size) requires approximately 20 times the CPU time needed for a single explicit step. Computation time is halved when the previous solution can be used as an initial guess. Another potential benefit of AIM not explored in this article is that this approach might lead to a natural way of partitioning a large model for the purpose of parallelisation. A parallel version of our transport model is already available (Coumou et al. 2008).

It is clear that the scheme can be applied to multiphase flow. The interested reader is referred to Matthäi et al. (2007a).

5 Conclusions

This article contributes a new higher-order accurate semi-implicit to implicit finite-element node-centred finite-volume method suitable for the simulation of transport processes on high-resolution, adaptively refined, hybrid element meshes representing rock fractures as discrete entities with internal degrees of freedom. The presented scheme overcomes the CFL constraint on time-step size which is prohibitive for explicit DFM fracture–rock matrix simulations because transport velocity varies over many orders of magnitude and tends to be largest in the smallest finite volume cells coinciding with fractures. By making time stepping implicit, we can exceed global CFL. Exceeding the CFL limit just makes the computational

results more dispersive. This numerical dispersion is evaluated through a comparison with a second-order accurate IMPES solution. We find that in spatially adaptively refined models of intensely fractured porous media studied here, the numerical dispersion incurred by the implicit large-time-step scheme is insignificant relative to the mechanical dispersion caused by the highly permeable fractures. This implies that transport calculations for multiple realisations can be conducted at low computational cost, if unstructured adaptively refined meshes are used as described in Paluszny et al. (2007). The numerical dispersion in the rock matrix is less pronounced when the fracture–matrix flux ratio is relatively high and the numerical error in simulations for higher q_f/q_m are much less than that for lower ones (Fig. 16). We further propose to use the super-CFL volume fraction of the model under consideration to achieve a goal-based numerical dispersion error. We use this target to find an optimal time discretisation/degree of CFL overstepping. For strongly fracture-dominated systems, we find that even for a single transport step to breakthrough, this error can be kept on the order of the fracture porosity%.

Acknowledgements We would like to thank the sponsors of the ITF project on 'Improved Simulation of Flow in Fractured and Faulted Reservoirs' for supporting this research. Mike Hohmeyer and Klaus Stüben have made important contributions in making available to this project the advanced unstructured gridding capabilities and the algebraic multigrid solver for systems of equations (SAMG). We are very grateful for the helpful and detailed comments provided by the reviewers.

References

Aziz, K.: Reservoir simulation grids: opportunities and problems. J. Petrol. Technol. **45**, 658–663 (1993)
Aziz, K., Settari, A.: Petroleum Reservoir Simulation, 476 pp. Applied Science Publishers, London (1979)
Baliga, B.R.: A control-volume based finite-element method for convective heat and mass transfer. Unpublished PhD thesis, University of Minnesota, Minneapolis (1978)
Baliga, B.R., Patankar, S.V.: A new finite-element formulation for convection-diffusion problems. Numer. Heat Transf. **3**, 393–409 (1980)
Belayneh, M., Matthäi, S.K., Geiger, S.: Numerical simulation of water injection into layered fractured carbonate reservoir analogues. Am. Assoc. Petrol. Geol. Bull. **90**, 1–21 (Oct 2006, in review)
Berkowitz, B., Scher, H.: Anomalous transport in random fracture networks. Phys. Rev. Lett. **79**(20), 4038–4041 (1997)
Cordes, C., Kinzelbach, W.: Continuous groundwater velocity fields and path lines in linear, bilinear, and trilinear finite elements. Water Resour. Res. **28**(11), 2903–2911 (1992)
Cortis, A., Birkholzer, J.: Continuous time random walk analysis of solute transport in fractured porous media. Water Resour. Res. **44**, W06414 (2008). doi:10.1029/2007WR006596
Coumou, D., Matthäi, S.K., Geiger, S., Driesner, T.: A parallel FE-FV scheme to solve fluid flow in complex geologic media. Comput. Geosci. **34**(12), 1697–1707 (2008). doi:10.1016/j.cageo.2007.11.010
Derschowitz, B., LaPointe, P., Eiben, T., Wei, L.: Integration of discrete feature network methods with conventional simulator approaches. SPE **49069**, 1–10 (1998)
Durlofsky, L.J.: A triangle based mixed finite element—finite volume technique for modeling two-phase flow through porous media. J. Comput. Phys. **105**, 252–266 (1993)
Eikemo, B., Lie, K.A., Eigestad, G.T., Dahle, H.K.: Discontinuous Galerkin methods for advective transport in single-continuum models of fractured media. Adv. Water Resour. **32**, 4 (2009)
Geiger, S., Roberts, S.G., Matthäi, S.K., Zoppou, C., Burri, A.: Combining finite element and finite volume methods for efficient multi-phase flow simulation in highly heterogeneous and geometrically complex porous media. Geofluids **4**, 284–299 (2004)
Gudonov, S.K.: The finite-difference method for the computation of discontinuous solutions of the equations of fluid dynamics. Math. Sb. **47**, 357–393 (1959)
Hoteit, H., Firoozabadi, A.: Multicomponent fluid flow by discontinuous Galerkin and mixed methods in unfractured and fractured media. Water Resour. Res. **41**, 69–73 (2005). doi:10.1029/2005WR004339
Huber, R., Helmig, R.: Multi-phase flow in heterogeneous porous media: a classical finite element method versus an implicit pressure-explicit saturation-based mixed finite element-finite volume approach. Int. J. Numer. Methods Fluids **29**, 899–920 (1999)

Huber, R., Helmig, R.: Node-centered finite volume discretizations for the numerical simulation of multiphase flow in heterogeneous porous media. Comput. Geosci. **4**, 141–164 (2000)
Huyakorn, P.S., Pinder, G.F.: Computational Methods in Subsurface Flow. Academic Press, London (1987)
Jiang, G.S., Tadmor, E.: Non-oscillatory central difference schemes for multidimensional hyperbolic conservation laws. SIAM J. Sci. Comput. **18**, 1892–1917 (1998)
Juanes, R., Samper, J., Molinero, J.: A general and efficient formulation of fractures and boundary conditions in the finite-element method. Int. J. Numer. Methods Eng. **54**, 1751–17774 (2002)
Karimi-Fard, K., Firoozabadi, A.: Numerical solution of water injection in fractured media using the discrete-fracture model and the Galerkin method. SPE Reserv. Eval. Eng. **6**(2), 117–126 (2003)
LeVeque, R.J.: Large time step shock-capturing techniques for scalar conservation laws. SIAM J. Numer. Anal. **19**(6), 1091–1109 (1982)
LeVeque, R.J.: Numerical Methods in Conservation Laws. Short Course Taught at the ETH Zürich. Birkhäuser Verlag, Basel (1987)
Matthäi, S.K., Belayneh, M.: Fluid flow partitioning between fractures and a permeable rock matrix. Geophys. Res. Lett. **31**(7), 5 pp. (2004)
Matthäi, S.K., Aydin, A., Pollard, D.D., Roberts, S.G.: Simulation of transient well-test signatures for geologically realistic faults in sandstone reservoirs. SPE J. **3**(1), 62–76, SPE38442 (1998)
Matthäi, S.K., Geiger, S., Roberts, S.G.: The Complex Systems Platform CSP5.0: User's Guide, 5th edn. ETH Research Reports, 150 pp. (2004)
Matthäi, S.K., Mezentsev, MA, Belayneh, MA.: Finite element-node-centred finite-volume two-phase-flow experiments with fractured rock represented by hybrid-element. SPE Reserv. Eval. Eng. **12**, 740–756 (2007a)
Matthäi, S.K., Geiger, S., Roberts, S.G., Paluszny, A., Belayneh, M., Burri, A., Mezentsev, A., Lu, H., Coumou, D., Driesner, T., Heinrich, C.A.: Numerical simulation of multi-phase fluid flow in structurally complex reservoirs. In: Jolley, S.J., Barr, D., Walsh, J.J., Knipe, R.J. (eds.) Structurally Complex Reservoirs, vol. 292, pp. 405–429. Geological Society, London, Special Publication (2007b)
Monteagudo, J.E.P., Firoozabadi, A.: Control-volume method for numerical simulation of two-phase flow in two- and three-dimensional discrete-fractured media. Water Resour. Res. **40**, W07405 (2004). doi:10.1029/2003WR002996
Mose, R., Siegel, P., Ackerer, P.: Application of the mixed hybrid finite element approximation in a groundwater flow model: luxury or necessity?. Water Resour. Res. **30**(11), 3001–3012 (1994)
Natvig, J.R., Lie, K.A.: Fast computation of multiphase flow in porous media by implicit discontinuous Galerkin schemes with optimal ordering of elements. J. Comput. Phys. **227**(24), 10108–10124 (2008). doi:10.1016/j.jcp.2008.08.024
Nessyahu, H., Tadmor, E.: Non-oscillatory central differencing for hyperbolic conservation laws. J. Comput. Phys. **87**, 408–463 (1988)
Nick, H.M., Schotting, R., Gutierrez-Neri, M., Johannsen, K.: Modeling transverse dispersion and variable density flow in porous media. Transp. Porous Media (2008). doi:10.1007/s11242-008-9277-x
Pain, C.C., Umpleby, A., de Oliveira, C., Goddard, A.: Tetrahedral mesh optimisation and adaptivity for steadystate and transient finite element calculations. Comput. Methods Appl. Mech. Eng. **190**(29–30), 3771–3796 (2001)
Pain, C.C., Eaton, M.D., Bowsher, J., Smedley-Stevenson, R.P., Umpleby, A.P., de Oliveira, C.R.E., Goddard, A.J.H.: Finite element based Riemann solvers for time-dependent and steady-state radiation transport. Transp. Theory Stat. Phys. **32**, 699–712 (2003)
Paluszny, A., Matthäi, S.K., Hohmeyer, H.: Hybrid finite element finite volume discretization of complex geologic structures and a new simulation workflow demonstrated on fractured rocks. Geofluids **7**, 186–208 (2007)
Ruge, J.W., Stüben, K.: Algebraic multigrid. In: McCormick, S.F. (ed.) Multigrid Methods: SIAM Frontiers in Applied Mathematics, vol. 3, pp. 73–130. SIAM, Philadelphia (1987)
Stüben, K.: Algebraic Multigrid (AMG): An Introduction with Applications. GMD Report 70, 127 pp. GMD—Forschungszentrum Informationstechnik GmbH, Sankt Augustin, Germany (1999)
Thomas, G.W., Thurnau, D.H.: The mathematical basis for the adaptive implicit method. SPE **10495**, 69–73 (1982)